

Effects of Berry curvature on ideal band magnetorotons

Jingtian Shi,¹ Jennifer Cano,^{2,3} and Nicolás Morales-Durán^{2,*}

¹*Materials Science Division, Argonne National Laboratory, Lemont, Illinois 60439, USA*

²*Center for Computational Quantum Physics, Flatiron Institute, New York, New York 10010, USA*

³*Department of Physics and Astronomy, Stony Brook University, Stony Brook, New York 11794, USA*

(Dated: March 21, 2025)

We investigate the many-body ground states in a family of fractionally-filled bands where the Berry curvature fluctuations can be tuned while maintaining ideal quantum geometry. We numerically find that the neutral gap of the fractional Chern insulator (FCI) ground state decreases as the Berry curvature becomes less homogeneous, ultimately driving an instability to a charge density wave. We derive an analytical model to explain this behavior by applying the single mode approximation to the ground state wave functions of the ideal band, from which we obtain a perturbative expression for the magnetoroton minimum. We extend our analysis to bands where the quantum geometry is weakly perturbed away from ideal and give examples where a less ideal band geometry results in a more stable FCI phase.

Introduction — Fractional Chern insulators (FCIs) are the analogs of fractional quantum Hall (FQH) states in the absence of magnetic field. They were proposed over a decade ago [1–6], but their realization remained elusive until recently, when observations in twisted transition metal dichalcogenide (TMD) homobilayers [7–10] and rhombohedral graphene multilayers [11] opened a new frontier in the field of topological order [12, 13]. Follow-up experimental studies have observed rich new phenomenology in both the TMD [14–17] and graphene [18, 19] platforms, giving rise to several puzzles regarding the nature of moiré FCIs. In this context, it is crucial to obtain a theoretical understanding of how electronic correlations in two-dimensional materials give rise to physics in the absence of a magnetic field that resembles – but at the same time reveals striking differences from – the FQH paradigm in Landau levels.

The observed FCIs are often studied theoretically by means of continuum models subject to periodic spatial modulations from the moiré superlattice [20]. The framework of quantum geometry [21–25] links those models to FQH physics through the notion of *ideal bands*, whose wave functions can be mapped to those of the lowest Landau level (LLL) precisely via a spatial modulation. Hamiltonians with ideal bands are appealing because, for a particular form of the electron-electron interactions, analytic many-body ground state wave functions can be obtained by generalizing the Laughlin construction [26, 27]. Examples of ideal band models include the chiral model of twisted bilayer graphene [28] and its multilayer generalizations [29, 30], Dirac and spin-1/2 Schrödinger particles in a periodic magnetic field [31, 32], the Kapit-Mueller model [33] and models with higher band touchings [34, 35]. Although real materials are not expected to be described by fine-tuned ideal band models, the experimental discovery of FQH physics over wide ranges of twist angle and displacement fields suggests that some moiré FCIs may be approximately described by perturbing away from an ideal band model. Thus, it is important

to understand how deviations from the limits of ideal geometry and constant Berry curvature impact the stability of putative FCI ground states. However, in generic models, finite band width, violations of ideal band geometry, and variations in Berry curvature often appear simultaneously, making it difficult to disentangle their effects on the ground state. In this work, we gain insight by isolating these effects.

We investigate the many-body physics of a family of ideal band models, that we refer to as Aharonov-Casher (AC) Hamiltonians. These models were introduced previously to approximate the continuum model for homobilayer TMDs [36, 37], but their many-body physics still remains to be fully explored [38]. The AC models have the advantage that the Berry curvature distribution of the topmost band can be tuned while maintaining the ideal quantum geometry and vanishing band width. This isolates the effect of non-homogeneous Berry curvature on the FCI that results when the top band is partially filled. Our exact diagonalization (ED) calculations show that for a realistic Coulomb interaction, the neutral gap of the FCI ground state decreases when Berry curvature fluctuations are increased, despite the band remaining ideal. We also observe that the magnitude of the magnetoroton gap depends on the location of the Berry curvature extrema in the original band. We explain these observations by exploiting the exact solvability of the AC Hamiltonian. Specifically, we apply the single mode approximation (SMA) in the limit of small Berry curvature inhomogeneity to obtain an analytic expression for the magnetoroton minimum, which agrees qualitatively with our numerics.

Finally, we study the many-body physics of band models with small violations from the ideal condition. Surprisingly, we find instances where sacrificing ideal geometry in favor of a more homogeneous Berry curvature increases the stability of the topologically-ordered phase. We relate this effect to realistic scenarios where FCIs have been experimentally observed.

Adiabatic and Aharonov-Casher Hamiltonians — We study the Hamiltonian

$$H_{\text{ad}} = H_{AC} + U = -\frac{1}{2m}\Pi_- \Pi_+ + U, \quad (1)$$

which, in a certain limit, approximates the continuum model of TMD homobilayers such as tMoTe₂ [36, 37, 39, 40]. In Eq. (1), $\Pi_{\pm} = (p_x + A_x) \pm i(p_y + A_y)$ are kinetic-momentum operators with $p_{\alpha} = -i\partial_{\alpha}$ for $\alpha = x, y$. $U = U(\mathbf{r})$ is a periodic potential (which we refer to as the residual potential), and $\mathbf{A}(\mathbf{r}) = (A_x(\mathbf{r}), A_y(\mathbf{r}))$ is a vector potential corresponding to a periodic magnetic field, $\nabla \times \mathbf{A}(\mathbf{r}) = B_0 + B(\mathbf{r})$, which we have split into a spatially uniform part with one flux quantum per unit cell, $B_0 = -1/\ell^2$, with ℓ the magnetic length, and a zero-average periodic piece $B(\mathbf{r})$. We assume $B(\mathbf{r})$ and $U(\mathbf{r})$ have the same periodicity, with Fourier expansions

$$B(\mathbf{r}) = \sum_{\mathbf{G}} B_{\mathbf{G}} e^{i\mathbf{G}\cdot\mathbf{r}}, \quad \text{and} \quad U(\mathbf{r}) = \sum_{\mathbf{G}} U_{\mathbf{G}} e^{i\mathbf{G}\cdot\mathbf{r}}, \quad (2)$$

where \mathbf{G} are their shared reciprocal lattice vectors.

Following [37] we refer to Eq. (1) as the *adiabatic Hamiltonian* and to its first term, H_{AC} , as the *Aharonov-Casher Hamiltonian*, which is known to have a manifold of zero-energy states for arbitrary magnetic field [31, 41]. When the magnetic field is periodic, the resulting zero-energy manifold can be understood as a quasi-Bloch band, which we will refer to as an AC band [37, 40]. These flat bands have ideal quantum geometry: more precisely, their quantum metric $g_{\mathbf{k}}^{ab}$ and Berry curvature $\Omega_{\mathbf{k}}$ satisfy the relation $\text{tr} g_{\mathbf{k}}^{ab} = |\Omega_{\mathbf{k}}|$, known as the trace condition [21, 22]. As a consequence, AC bands can support Laughlin-like ground states whose analytic wavefunctions are related to those of the FQH effect [24, 42, 43].

The wave functions of the AC band can be written as

$$\psi^{AC}(\mathbf{r}) = f(z) e^{-\frac{|z|^2}{4\ell^2} + \chi(\mathbf{r})} = \psi^{LLL}(\mathbf{r}) e^{\chi(\mathbf{r})}, \quad (3)$$

where $z = x + iy$, f is a holomorphic function, $\chi(\mathbf{r})$ is a real periodic function related to the magnetic field by $\nabla^2 \chi(\mathbf{r}) = B(\mathbf{r})$ and $\psi^{LLL}(\mathbf{r})$ is a lowest Landau level wave function. Eq. (3) defines a mapping between LLL wave functions and AC wave functions, from which we can define a magnetic quasi-Bloch basis for the AC band $|\psi_{\mathbf{k}}^{AC}\rangle = e^{\chi(\mathbf{r})} |\psi_{\mathbf{k}}^{LLL}\rangle$, in terms of the quasi-Bloch states of the LLL, $|\psi_{\mathbf{k}}^{LLL}\rangle$ [44–47]. The Berry curvature of the AC band is given by [24, 37]

$$\begin{aligned} \Omega_{\mathbf{k}} &= \frac{2\pi}{A_{\text{BZ}}} + \frac{1}{2} \nabla_{\mathbf{k}}^2 \ln \langle \psi_{\mathbf{k}}^{AC} | \psi_{\mathbf{k}}^{AC} \rangle \\ &= \Omega_0 + \frac{1}{2} \nabla_{\mathbf{k}}^2 \ln \left(\sum_{\mathbf{G}} \Phi_{\mathbf{G}} \langle \psi_{\mathbf{k}}^{LLL} | e^{i\mathbf{G}\cdot\hat{\mathbf{r}}} | \psi_{\mathbf{k}}^{LLL} \rangle \right), \end{aligned} \quad (4)$$

where A_{BZ} is the area of the Brillouin zone and $\Phi_{\mathbf{G}}$ are the Fourier coefficients of the function $e^{2\chi(\mathbf{r})}$. Eq. (4)

shows that the Berry curvature distribution of the AC band can be controlled by tuning $B(\mathbf{r})$, while the quantum geometry is known to remain ideal [24]. When $U(\mathbf{r}) \neq 0$ in Eq. (1), the topmost band is no longer ideal, and we will refer to it as an adiabatic band. However, we expect the FQH-like ground state of the AC Hamiltonian to survive for perturbative strengths of the residual potential.

Many-body calculations — We fractionally fill the highest energy band of the Hamiltonian in Eq. (1) with spinless holes and add band-projected un-screened Coulomb interactions, $V(\mathbf{r}) = e^2/|\mathbf{r}|$. We then obtain the many-body spectrum by performing exact diagonalization. We choose parameters comparable to those of twisted TMDs: specifically, we set the dimensionless strength of the Coulomb interaction to $e^2/\varepsilon\ell = 3.408\omega_c$, with the cyclotron frequency given by $\omega_c = 1/m\ell^2$, corresponding to continuum model parameters from [48], and dielectric constant $\varepsilon = 10$. The many-body Hamiltonian is

$$H = \sum_{\mathbf{k}} \epsilon_{\mathbf{k}} c_{\mathbf{k}}^{\dagger} c_{\mathbf{k}} + \frac{1}{2} \sum_{\substack{\mathbf{k}_i, \mathbf{k}_j \\ \mathbf{k}_k, \mathbf{k}_l}} V_{ijkl} c_{\mathbf{k}_i}^{\dagger} c_{\mathbf{k}_j}^{\dagger} c_{\mathbf{k}_l} c_{\mathbf{k}_k}, \quad (5)$$

where $\epsilon_{\mathbf{k}}$ are single-particle energies, $c_{\mathbf{k}}^{\dagger} (c_{\mathbf{k}})$ creates (destroys) a spinless hole with momentum \mathbf{k} and V_{ijkl} is a two-particle matrix element; see the supplemental material (SM) [49] for details on how the interaction matrix elements are obtained.

For simplicity we assume both functions in Eq. (2) have six-fold symmetry and truncate them to the first shell of reciprocal lattice vectors, with magnitude $|\mathbf{G}| = G_0$. In this approximation, the first-shell harmonics, denoted B_1 and U_1 , serve as tuning parameters that control the Berry curvature distribution and deviations from ideal geometry of the topmost band of Eq. (1). In the SM [49] we justify this approximation by showing that the higher harmonics B_2, U_2, \dots only weakly affect the many-body spectra. In the following, B_1 has units of $1/\ell^2$ and U_1 has units of ω_c . For calculations presented in the main text, we focus on filling $\nu = 1/3$; in the SM [49] we also consider $\nu = 2/3$. We observe particle-hole asymmetry with respect to half-filling for both $B_1 \neq 0$ and $U_1 \neq 0$, which is expected due to the non-trivial quantum geometry of the topmost band [50, 51].

Effects of inhomogeneous Berry curvature on ideal band FCIs — We first study the many-body spectrum of AC bands, which are obtained from the Hamiltonian in Eq. (1) with $U(\mathbf{r}) = 0$. Despite the AC band being ideal, an exact zero-energy Laughlin-like ground state at $\nu = 1/3$ is not required, as the interaction we chose contains terms beyond the first Haldane pseudopotential. While we observe an FCI ground state for $B(\mathbf{r}) = 0$, strong Berry curvature inhomogeneity drives a transition out of that state. Previous studies of this transition simultaneously included deviations from the ideal band condition [52–55]. The unique aspect of our work is that

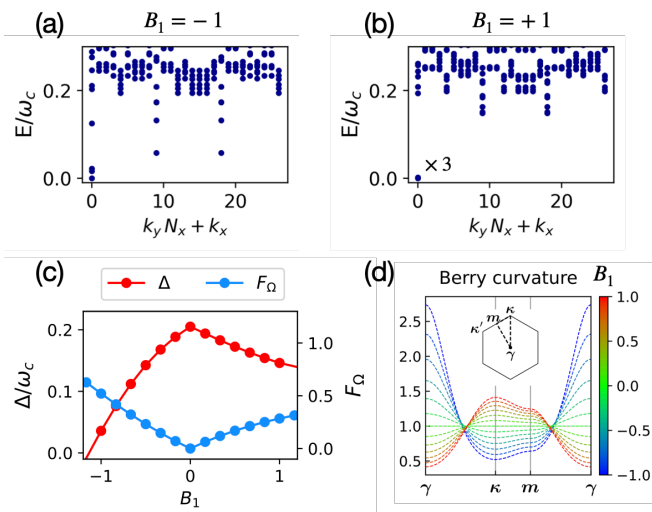


FIG. 1. (a)-(b) Many-body spectra at filling $\nu = 1/3$ for an AC band with $B_1 = -1$ and $B_1 = +1$, respectively. (c) Dependence of the magnetoroton gap Δ at filling $\nu = 1/3$ (red) and Berry curvature standard deviation F_Ω (see Eq. (6)) of the AC band (blue) as a function of B_1 . (d) Berry curvature distribution of the AC band as a function of B_1 . Calculations were performed for systems with 27 unit cells.

we have isolated the effect of Berry curvature fluctuations from deviations from idealness on the nature of the ground state. We achieve this by tuning B_1 , which determines the Berry curvature of the ideal AC band via Eq. (4).

Figs. 1(a)-(b) show the many-body spectrum at filling $\nu = 1/3$ for AC bands with $B_1 = -1$ and $B_1 = +1$, respectively. For both calculations the ground state remains in the same universality class, with three quasi-degenerate ground states in the same momentum sector, but the Berry curvature distribution significantly affects the low-energy excitation spectrum. Specifically, the gap to the lowest neutral magnetoroton excitation [56] at κ/κ' is much smaller when B_1 is negative. Fig. 1(c) shows this asymmetry explicitly by plotting the neutral gap, Δ , as a function of B_1 ; see SM [49] for the definition of Δ .

We quantify Berry curvature inhomogeneity of the band through

$$F_\Omega = \sqrt{\int_{\text{BZ}} \frac{d^2 \mathbf{k}}{A_{\text{BZ}}} \left(\frac{\Omega_{\mathbf{k}}}{\Omega_0} - C \right)^2}, \quad (6)$$

where C is the Chern number. Fig. 1(c) shows F_Ω as a function of B_1 , while Fig. 1(d) shows the Berry curvature distribution of the AC band across the Brillouin zone, as a function of B_1 . The location of the Berry curvature peaks in Fig. 1(d) follows from a perturbative expansion

of Eq. (4) in B_1 , detailed in the SM [49],

$$\Omega_{\mathbf{k}} \approx \Omega_0 - \frac{4\pi\ell^2 B_1 e^{-\frac{G_0^2 \ell^2}{4}}}{\sqrt{3}G_0^2} \sum_{j=1}^6 e^{i\mathbf{k} \cdot \mathbf{R}_j} + O(B_1^2), \quad (7)$$

here \mathbf{R}_j are the six first-shell lattice vectors determining the periodicity of $B(\mathbf{r})$. We see that for $B_1 > 0$, Eq. (7) predicts that the Berry curvature has peaks at κ/κ' while for $B_1 < 0$ it predicts a single peak at γ . However, Fig. 1(d) also reveals an asymmetry in the magnitude of peaks/troughs beyond the linear expansion in Eq. (7).

Fig. 1(c) shows that the maximum magnetoroton gap Δ is attained for homogeneous Berry curvature, *i.e.* $B_1 = 0$, and that fluctuations in Berry curvature lead to an approximately linear decrease in Δ where the slope depends on the sign of B_1 . To understand this behavior, we use the single mode approximation to define low-energy neutral excitations on top of the AC ground state. In the limit $B_1 \ll 1$ we apply degenerate perturbation theory to the magnetoroton states at κ/κ' , where the minimum happens, and obtain an expression for the AC magnetoroton gap in terms of the LLL gap, denoted Δ^{LLL} :

$$\Delta(\kappa) \approx \begin{cases} \Delta^{LLL}(\kappa) - (\alpha + \beta) |B_1|, & \text{for } B_1 > 0. \\ \Delta^{LLL}(\kappa) - 2\alpha |B_1|, & \text{for } B_1 < 0. \end{cases} \quad (8)$$

See the SM [49] for details on our magnetoroton model for AC bands and expressions for the coefficients α and β , that satisfy $\alpha > 0$ and $\alpha \neq \beta$, according to our numerics. Eq. (8) captures the asymmetric behavior of Δ with respect to $B_1 = 0$ observed in Fig. 1(c). For completeness, in the SM [49] we present momentum occupation plots $n_{\mathbf{k}}$, which show a smaller occupation in regions of the Brillouin zone where the Berry curvature is peaked, in agreement with [51]. Ultimately the large inhomogeneity in $\Omega_{\mathbf{k}}$, which translates into a large F_Ω , leads to a charge density wave (CDW) with $\Delta < 0$, as can be seen in Fig. 1(c).

Effects of inhomogeneous Berry curvature on adiabatic band FCIs — In contrast to the AC bands studied in the previous section, bands that describe the low-energy physics of two-dimensional materials generically have a non-vanishing dispersion and do not satisfy the trace condition. To recover that scenario, we restore the residual potential $U(\mathbf{r})$ in the adiabatic Hamiltonian, Eq (1), yielding a non-ideal topmost band. Tuning the parameter U_1 will simultaneously change the Berry curvature distribution, destroy the trace condition and introduce a finite band width. These effects together ultimately determine the interacting ground state.

Fig. 2(a) shows the evolution of Δ as a function of U_1 for adiabatic bands with different B_1 , while Fig. 2(b) shows the same quantity, but neglecting the kinetic energy in the ED calculations. The gap Δ is asymmetric with respect to the sign of U_1 , which is more pronounced in Fig. 2(b). The asymmetry indicates that a triangular

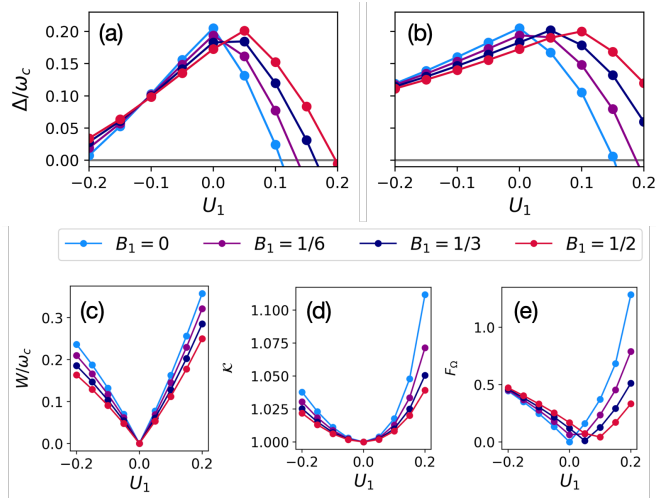


FIG. 2. Magnetoroton gap Δ as a function of U_1 for different values of B_1 . We compare calculations (a) including and (b) neglecting the band width induced by U_1 . (c) Band width W , (d) quantum weight \mathcal{K} (see main text) and (e) Berry curvature standard deviation for each adiabatic band, as a function of U_1 .

periodic potential with peaks at the AA positions in the unit cell ($U_1 > 0$) is less favorable for realizing an FCI than a honeycomb potential with peaks at the AB/BA positions ($U_1 < 0$), in agreement with [57]. Figs. 2(c)-(e) show the band width W , quantum weight \mathcal{K} and Berry curvature inhomogeneity F_Ω , respectively, for each adiabatic band. The quantum weight is defined as the Brillouin zone average of $\text{tr}g_{\mathbf{k}}$ divided by 2π [58–60], which equals the Chern number C for ideal bands and thus measures the deviation from ideal quantum geometry.

Both W and \mathcal{K} are larger for $U_1 > 0$ than for $U_1 < 0$ and contribute to the reduced stability of the FCI. A surprising observation is that for fixed $B_1 > 0$, the largest many-body gap occurs not for the ideal band ($U_1 = 0$), but for a non-ideal band with finite $U_1 > 0$. This results in a larger region of FCI stability for bands with $B_1 \neq 0$ and can be explained from the behavior of F_Ω : the Berry curvature induced by $U_1 > 0$ and $B_1 > 0$ is peaked in opposite locations in the Brillouin zone, so that the adiabatic Hamiltonian with finite U_1, B_1 has smaller Berry curvature fluctuations than when either term separately vanishes, as can be seen in Fig. 2(e). In the SM [49] we present plots for the Berry curvatures of the adiabatic bands to illustrate this behavior. We note that in our analysis it is crucial that U_1 is small, in contrast to previously studied topological band models where flattening the Berry curvature can destabilize the FCI phase [61] but the trace condition is strongly violated.

The adiabatic Hamiltonian studied here gives insight into the stability of FCIs in twisted homobilayer TMDs. Specifically, the continuum model for the latter can be mapped to Eq. (1) by replacing the layer degree of free-

dom by a periodic magnetic field and a periodic potential, and discarding all but the lowest harmonics of $B(\mathbf{r})$ and $U(\mathbf{r})$ [37]. In our convention, this approximation applied to a particular model of twisted MoTe_2 (t MoTe_2) [62] yields $B_1 = 0.22 [1/\ell^2]$, which is independent of twist angle, and $U_1 = -7.36 + 0.57 (\theta[\text{deg}])^2$ in units of meV. By converting to ω_c units, we obtain that for the range $2.5^\circ - 5^\circ$, the value of U_1 goes from $U_1 = -0.27 [\omega_c]$ to $U_1 = 0.13 [\omega_c]$, justifying the parameter ranges that we have chosen for our study. Our results in Fig. 2 are a possible explanation for why the FCI phase in semiconductor moiré systems remains stable over a large range of twist angles, as numerically [62–67] and experimentally [7–10] observed, and predict that for angles above the magic angle, where the topmost continuum band is closest to flat and ideal, the FCI ground state will be more robust.

Discussion — We have numerically and analytically investigated the effect of Berry curvature fluctuations on the magnetoroton gap of FCIs in ideal and near-ideal bands, in the presence of a realistic Coulomb interaction. In the limit of small Berry curvature fluctuations, we derive a perturbative expression for the magnetoroton minimum in terms of the LLL magnetoroton gap, which captures the asymmetry of the neutral FCI gap with respect to the momentum-space position of the Berry curvature maxima. This powerful analytical result sheds light on the properties of Berry curvature that favor the stability of FCI ground states and is complementary to other approaches to address FCI excitations [56, 68–77]. We have used our results to explain the large region of stability for topologically-ordered phases in twisted TMDs, where the quantum geometry is not ideal anymore.

We focused on spinless fermions, for which the FCI is destabilized by neutral magnetoroton modes. When spin or orbital degrees of freedom are taken into account, other candidate phases become competitive. It will be interesting to investigate the role of Berry curvature fluctuations in such situations, where spin- and valley-unpolarized topological phases could be favored over a ferromagnetic ground state [52, 78]. Our band-projected results yield finite and comparable magnetoroton gaps for $\nu = 1/3$ and $\nu = 2/3$ (See SM [49].) This is in contrast to experiments in t MoTe_2 , where the FCI state is robust at $\nu = 2/3$ and absent at $\nu = 1/3$, pointing to the importance of remote band mixing in realistic systems, as discussed by other authors [79, 80]. We leave the analysis of remote band effects and valley degrees of freedom in our model for future work.

Acknowledgements: The authors are grateful to Allan H. MacDonald for related collaborations and inspiring discussions. NMD thanks Valerio Peri, Pawel Potasz, Aidan Reddy, Nicolas Regnault, Cécile Repellin and Jie Wang for discussions. JS thanks Xiaodong Hu and Xiaoyang Shen for helpful interactions. This research was

supported in part by grant NSF PHY-2309135 to the Kavli Institute for Theoretical Physics (KITP). JS acknowledges support by the US Department of Energy, Office of Science, Basic Energy Sciences, Materials Sciences and Engineering Division. JC acknowledges support from the Air Force Office of Scientific Research under Grant No. FA9550-24-1-0222 and from the Alfred P. Sloan Foundation through a Sloan Research Fellowship. We acknowledge computational resources provided by the Texas Advanced Computing Center (TACC). The Flatiron Institute is a division of the Simons Foundation.

Author contributions: NMD and JS designed the project and JC supervised it. JS calculated the non-interacting band structures and provided the basis wave functions for exact diagonalization; NMD and JC developed the magnetoroton theory; NMD performed the ED calculations and wrote the paper with input from all authors.

* nmoralesduran@flatironinstitute.org

- [1] E. Tang, J.-W. Mei, and X.-G. Wen, *Phys. Rev. Lett.* **106**, 236802 (2011).
- [2] K. Sun, Z. Gu, H. Katsura, and S. Das Sarma, *Phys. Rev. Lett.* **106**, 236803 (2011).
- [3] T. Neupert, L. Santos, C. Chamon, and C. Mudry, *Phys. Rev. Lett.* **106**, 236804 (2011).
- [4] D. N. Sheng, Z.-C. Gu, K. Sun, and L. Sheng, *Nature Communications* **2**, 389 (2011).
- [5] N. Regnault and B. A. Bernevig, *Phys. Rev. X* **1**, 021014 (2011).
- [6] Y.-L. Wu, B. A. Bernevig, and N. Regnault, *Phys. Rev. B* **85**, 075116 (2012).
- [7] J. Cai, E. Anderson, C. Wang, X. Zhang, X. Liu, W. Holtzmann, Y. Zhang, F. Fan, T. Taniguchi, K. Watanabe, Y. Ran, T. Cao, L. Fu, D. Xiao, W. Yao, and X. Xu, *Nature* **622**, 63 (2023).
- [8] Y. Zeng, Z. Xia, K. Kang, J. Zhu, P. Knüppel, C. Vaswani, K. Watanabe, T. Taniguchi, K. F. Mak, and J. Shan, *Nature* **622**, 69 (2023).
- [9] H. Park, J. Cai, E. Anderson, Y. Zhang, J. Zhu, X. Liu, C. Wang, W. Holtzmann, C. Hu, Z. Liu, T. Taniguchi, K. Watanabe, J.-H. Chu, T. Cao, L. Fu, W. Yao, C.-Z. Chang, D. Cobden, D. Xiao, and X. Xu, *Nature* **622**, 74 (2023).
- [10] F. Xu, Z. Sun, T. Jia, C. Liu, C. Xu, C. Li, Y. Gu, K. Watanabe, T. Taniguchi, B. Tong, J. Jia, Z. Shi, S. Jiang, Y. Zhang, X. Liu, and T. Li, *Phys. Rev. X* **13**, 031037 (2023).
- [11] Z. Lu, T. Han, Y. Yao, A. P. Reddy, J. Yang, J. Seo, K. Watanabe, T. Taniguchi, L. Fu, and L. Ju, *Nature* **626**, 759 (2024).
- [12] L. Ju, A. H. MacDonald, K. F. Mak, J. Shan, and X. Xu, *Nature Reviews Materials* **9**, 455 (2024).
- [13] N. Morales-Durán, J. Shi, and A. H. MacDonald, *Nature Reviews Physics* **6**, 349 (2024).
- [14] K. Kang, B. Shen, Y. Qiu, Y. Zeng, Z. Xia, K. Watanabe, T. Taniguchi, J. Shan, and K. F. Mak, *Nature* **628**, 522 (2024).
- [15] K. Kang, Y. Qiu, B. Shen, K. Lee, Z. Xia, Y. Zeng, K. Watanabe, T. Taniguchi, J. Shan, and K. F. Mak, “Time-reversal symmetry breaking fractional quantum spin hall insulator in moiré mote2,” (2025), arXiv:2501.02525 [cond-mat.mes-hall].
- [16] H. Park, J. Cai, E. Anderson, X.-W. Zhang, X. Liu, W. Holtzmann, W. Li, C. Wang, C. Hu, Y. Zhao, T. Taniguchi, K. Watanabe, J. Yang, D. Cobden, J.-H. Chu, N. Regnault, B. A. Bernevig, L. Fu, T. Cao, D. Xiao, and X. Xu, “Ferromagnetism and topology of the higher flat band in a fractional chern insulator,” (2024), arXiv:2406.09591 [cond-mat.mes-hall].
- [17] Y. Wang, J. Choe, E. Anderson, W. Li, J. Ingham, E. A. Arsenault, Y. Li, X. Hu, T. Taniguchi, K. Watanabe, X. Roy, D. Basov, D. Xiao, R. Queiroz, J. C. Hone, X. Xu, and X. Y. Zhu, “Hidden states and dynamics of fractional fillings in tmote2 moiré superlattices,” (2025), arXiv:2502.21153 [cond-mat.str-el].
- [18] Z. Lu, T. Han, Y. Yao, J. Yang, J. Seo, L. Shi, S. Ye, K. Watanabe, T. Taniguchi, and L. Ju, “Extended quantum anomalous hall states in graphene/hbn moiré superlattices,” (2024), arXiv:2408.10203 [cond-mat.mes-hall].
- [19] Y. Choi, Y. Choi, M. Valentini, C. L. Patterson, L. F. W. Holleis, O. I. Sheekey, H. Stoyanov, X. Cheng, T. Taniguchi, K. Watanabe, and A. F. Young, “Electric field control of superconductivity and quantized anomalous hall effects in rhombohedral tetralayer graphene,” (2024), arXiv:2408.12584 [cond-mat.mes-hall].
- [20] F. Wu, T. Lovorn, E. Tutuc, I. Martin, and A. H. MacDonald, *Phys. Rev. Lett.* **122**, 086402 (2019).
- [21] R. Roy, *Phys. Rev. B* **90**, 165139 (2014).
- [22] T. S. Jackson, G. Möller, and R. Roy, *Nat Commun* **6**, 8629 (2015).
- [23] J. Wang, Y. Zheng, A. J. Millis, and J. Cano, *Phys. Rev. Research* **3**, 023155 (2021).
- [24] J. Wang, J. Cano, A. J. Millis, Z. Liu, and B. Yang, *Phys. Rev. Lett.* **127**, 246403 (2021).
- [25] J. Wang, S. Klevtsov, and Z. Liu, *Phys. Rev. Research* **5**, 023167 (2023).
- [26] R. B. Laughlin, *Phys. Rev. Lett.* **50**, 1395 (1983).
- [27] S. A. Trugman and S. Kivelson, *Phys. Rev. B* **31**, 5280 (1985).
- [28] G. Tarnopolsky, A. J. Kruchkov, and A. Vishwanath, *Phys. Rev. Lett.* **122**, 106405 (2019).
- [29] J. Wang and Z. Liu, *Phys. Rev. Lett.* **128**, 176403 (2022).
- [30] P. J. Ledwith, A. Vishwanath, and E. Khalaf, *Phys. Rev. Lett.* **128**, 176404 (2022).
- [31] A. Dubrovin and S. P. Novikov, *Sov. Phys. JETP* **52**, 511 (1980).
- [32] J. Dong, J. Wang, and L. Fu, “Dirac electron under periodic magnetic field: Platform for fractional chern insulator and generalized wigner crystal,” (2022), arXiv:2208.10516 [cond-mat.mes-hall].
- [33] E. Kapit and E. Mueller, *Phys. Rev. Lett.* **105**, 215303 (2010).
- [34] X. Wan, S. Sarkar, S.-Z. Lin, and K. Sun, *Phys. Rev. Lett.* **130**, 216401 (2023).
- [35] S. Sarkar, X. Wan, Y. Zhang, and K. Sun, “Ideal topological flat bands in chiral symmetric moiré systems from non-holomorphic functions,” (2024), arXiv:2408.12555 [cond-mat.mes-hall].
- [36] N. Morales-Durán, N. Wei, J. Shi, and A. H. MacDonald, *Phys. Rev. Lett.* **132**, 096602 (2024).
- [37] J. Shi, N. Morales-Durán, E. Khalaf, and A. H. Mac-

- Donald, Phys. Rev. B **110**, 035130 (2024).
- [38] B. Li and F. Wu, Phys. Rev. B **111**, 125122 (2025).
- [39] D. Zhai and W. Yao, Phys. Rev. Mater. **4**, 094002 (2020).
- [40] V. Crépel, N. Regnault, and R. Queiroz, Commun Phys **7**, 146 (2024).
- [41] Y. Aharonov and A. Casher, Phys. Rev. A **19**, 2461 (1979).
- [42] P. J. Ledwith, G. Tarnopolsky, E. Khalaf, and A. Vishwanath, Phys. Rev. Research **2**, 023237 (2020).
- [43] P. J. Ledwith, A. Vishwanath, and D. E. Parker, Phys. Rev. B **108**, 205144 (2023).
- [44] R. Ferrari, Phys. Rev. B **42**, 4598 (1990).
- [45] R. Ferrari, Int. J. Mod. Phys. B **09**, 3333 (1995).
- [46] F. D. M. Haldane, Journal of Mathematical Physics **59**, 071901 (2018).
- [47] J. Wang, S. D. Geraedts, E. H. Rezayi, and F. D. M. Haldane, Phys. Rev. B **99**, 125123 (2019).
- [48] T. Devakul, V. Crépel, Y. Zhang, and L. Fu, Nat Commun **12**, 6730 (2021).
- [49] See Supplemental Material for (a) Details on the many-body numerics (b) Details on the analytic calculation of the magnetoroton gap.
- [50] A. M. Läuchli, Z. Liu, E. J. Bergholtz, and R. Moessner, Phys. Rev. Lett. **111**, 126802 (2013).
- [51] A. Abouelkomsan, K. Yang, and E. J. Bergholtz, Phys. Rev. Research **5**, L012015 (2023).
- [52] C. Repellin and T. Senthil, Phys. Rev. Res. **2**, 023238 (2020).
- [53] P. Wilhelm, T. C. Lang, and A. M. Läuchli, Phys. Rev. B **103**, 125406 (2021).
- [54] P. H. Wilhelm, A. M. Läuchli, and M. S. Scheurer, Phys. Rev. Res. **6**, 043240 (2024).
- [55] G. Shavit and Y. Oreg, Phys. Rev. Lett. **133**, 156504 (2024).
- [56] C. Repellin, T. Neupert, Z. Papić, and N. Regnault, Phys. Rev. B **90**, 045114 (2014).
- [57] B. M. Kousa, N. Morales-Durán, T. M. R. Wolf, E. Khalaf, and A. H. MacDonald, “Theory of magnetoroton bands in moiré materials,” (2025).
- [58] Y. Onishi and L. Fu, Phys. Rev. X **14**, 011052 (2024).
- [59] Y. Onishi and L. Fu, Phys. Rev. Lett. **133**, 206602 (2024).
- [60] Y. Onishi and L. Fu, “Quantum weight: A fundamental property of quantum many-body systems,” (2024), arXiv:2406.06783 [cond-mat.str-el].
- [61] D. Varjas, A. Abouelkomsan, K. Yang, and E. J. Bergholtz, SciPost Phys. **12**, 118 (2022).
- [62] C. Wang, X.-W. Zhang, X. Liu, Y. He, X. Xu, Y. Ran, T. Cao, and D. Xiao, Phys. Rev. Lett. **132**, 036501 (2024).
- [63] J. Yu, J. Herzog-Arbeitman, M. Wang, O. Vafek, B. A. Bernevig, and N. Regnault, Phys. Rev. B **109**, 045147 (2024).
- [64] A. P. Reddy and L. Fu, Phys. Rev. B **108**, 245159 (2023).
- [65] A. P. Reddy, F. Alsallom, Y. Zhang, T. Devakul, and L. Fu, Phys. Rev. B **108**, 085117 (2023).
- [66] N. Morales-Durán, J. Wang, G. R. Schleder, M. Angeli, Z. Zhu, E. Kaxiras, C. Repellin, and J. Cano, Phys. Rev. Research **5**, L032022 (2023).
- [67] H. Li, U. Kumar, K. Sun, and S.-Z. Lin, Phys. Rev. Research **3**, L032070 (2021).
- [68] H. Lu, H.-Q. Wu, B.-B. Chen, K. Sun, and Z. Y. Meng, “Interaction-driven roton condensation in $c = 2/3$ fractional quantum anomalous Hall state,” (2024), arXiv:2403.03258 [cond-mat.str-el].
- [69] H. Lu, B.-B. Chen, H.-Q. Wu, K. Sun, and Z. Y. Meng, Phys. Rev. Lett. **132**, 236502 (2024).
- [70] H. Lu, H.-Q. Wu, B.-B. Chen, and Z. Y. Meng, “From a fractional quantum anomalous Hall state to a smectic state with equal Hall conductance,” (2024), arXiv:2404.06745 [cond-mat.str-el].
- [71] X. Shen, C. Wang, X. Hu, R. Guo, H. Yao, C. Wang, W. Duan, and Y. Xu, “Magnetorotons in moiré fractional Chern insulators,” (2024), arXiv:2412.01211 [cond-mat.str-el].
- [72] M. Long, H. Lu, H.-Q. Wu, and Z. Y. Meng, “Spectra of magnetoroton and chiral graviton modes of fractional Chern insulator,” (2025), arXiv:2501.00247 [cond-mat.str-el].
- [73] X. Hu, D. Xiao, and Y. Ran, Phys. Rev. B **109**, 245125 (2024).
- [74] F. Wu and A. H. MacDonald, Phys. Rev. B **94**, 241108 (2016).
- [75] T. M. R. Wolf, Y.-C. Chao, A. H. MacDonald, and J. J. Su, “Intraband collective excitations in fractional chern insulators are dark,” (2024), arXiv:2406.10709 [cond-mat.str-el].
- [76] J. F. Mendez-Valderrama, D. Mao, and D. Chowdhury, Phys. Rev. Lett. **133**, 196501 (2024).
- [77] N. Paul, A. Abouelkomsan, A. Reddy, and L. Fu, “Shining light on collective modes in moiré fractional chern insulators,” (2025), arXiv:2502.17569 [cond-mat.mes-hall].
- [78] Y. H. Kwan, G. Wagner, J. Yu, A. K. Dagnino, Y. Jiang, X. Xu, B. A. Bernevig, T. Neupert, and N. Regnault, “When could abelian fractional topological insulators exist in twisted mote₂ (and other systems),” (2024), arXiv:2407.02560 [cond-mat.str-el].
- [79] A. Abouelkomsan, A. P. Reddy, L. Fu, and E. J. Bergholtz, Phys. Rev. B **109**, L121107 (2024).
- [80] J. Yu, J. Herzog-Arbeitman, Y. H. Kwan, N. Regnault, and B. A. Bernevig, “Moiré fractional chern insulators iv: Fluctuation-driven collapse of fcis in multi-band exact diagonalization calculations on rhombohedral graphene,” (2024), arXiv:2407.13770 [cond-mat.str-el].
- [81] B. A. Bernevig and N. Regnault, Phys. Rev. B **85**, 075128 (2012).
- [82] S. M. Girvin, A. H. MacDonald, and P. M. Platzman, Phys. Rev. Lett. **54**, 581 (1985).
- [83] S. M. Girvin, A. H. MacDonald, and P. M. Platzman, Phys. Rev. B **33**, 2481 (1986).

**SUPPLEMENTAL MATERIAL FOR “EFFECTS OF BERRY CURVATURE ON IDEAL BAND
MAGNETOROTONS”**

Details on many-Body Calculation Methods

A natural basis in which to write the eigenstates of the Hamiltonian given by Eq. (1) in the main text is that of the Landau levels of the magnetic field B_0 ,

$$\psi_{n,\mathbf{k}}(\mathbf{r}) = \sum_m c_{m,\mathbf{k}}^n \psi_{\mathbf{k}}^{mLL}(\mathbf{r}), \quad (9)$$

where n is a band index, m a Landau level index, and \mathbf{k} is the quasi-Bloch momentum that characterizes the magnetic translational eigenstates. The coefficients $c_{m,\mathbf{k}}^n$ can be obtained by a diagonalization scheme developed in Ref. [37]. In order to obtain the many-body spectrum of Eq. (1) we require to compute the two-particle interaction matrix elements between the eigenstates defined by Eq. (9). The twisted Bloch periodicity of these single-particle eigenstates due to the magnetic flux is

$$\psi_{n,\mathbf{k}}(\mathbf{r} + \mathbf{R}) = \eta_{\mathbf{R}} e^{i(\mathbf{k} \cdot \mathbf{R} + \frac{\mathbf{R} \times \mathbf{r}}{2})} \psi_{n,\mathbf{k}}(\mathbf{r}), \quad (10)$$

(here \mathbf{R} is arbitrary lattice vector and $\eta_{\mathbf{R}}$ is the parity signature, *i.e.*, 1 if $\mathbf{R}/2$ is in the Bravais lattice and -1 otherwise), which complicates the direct evaluation of interaction matrix elements. For that reason we introduce an auxiliary spinor field $u_s(\mathbf{r})$ which cancels out the magnetic twist to give a perfect Bloch state:

$$\phi_{n,\mathbf{k}s}(\mathbf{r}) = \psi_{n,\mathbf{k}}(\mathbf{r}) u_s(\mathbf{r}) = \sum_{\mathbf{G}} z_{n,\mathbf{k},\mathbf{G},s} e^{i(\mathbf{k} + \mathbf{G}) \cdot \mathbf{r}}, \quad (11)$$

where $s = +, -$ is a pseudospin index and \mathbf{G} is a reciprocal lattice vector. We emphasize here that the pseudospin index s is purely auxiliary and does not need to be associated with any physical flavor. The choice of $u_s(\mathbf{r})$ has large freedom: as long as it has the proper twisted periodicity and normalization $|\mathbf{u}(\mathbf{r})|^2 = 1$, the determination of interaction matrix elements can be carried out in the Bloch basis defined in Eq. (11), which lives in the Hilbert space of the continuum model of twisted homobilayer TMDs [20]. This mapping also facilitates comparison with many-body numerical calculations using realistic continuum models of WSe₂ or MoTe₂ with parameters obtained from DFT [38]. Importantly, we note that the effective interlayer and intralayer interactions in our “fictitious bilayer” have to be both identical to the original interaction, thereby ensuring that the interaction matrix elements do not depend on the details of $u_s(\mathbf{r})$.

We now describe the specific choice of $u_s(\mathbf{r})$ for all our many-body calculations, which derives from the adiabatic approximation of twisted homobilayer TMDs [36, 37]. We locally diagonalize the layer-resolved moiré potential:

$$\Delta(\mathbf{r}) = \Delta_0(\mathbf{r}) + \boldsymbol{\sigma} \cdot \boldsymbol{\Delta}(\mathbf{r}), \quad (12a)$$

$$\Delta(\mathbf{r}) \tilde{\mathbf{u}}(\mathbf{r}) = (\Delta_0(\mathbf{r}) + |\boldsymbol{\Delta}(\mathbf{r})|) \tilde{\mathbf{u}}(\mathbf{r}), \quad (12b)$$

where $\boldsymbol{\sigma} = (\sigma^x, \sigma^y, \sigma^z)$ is the layer-pseudospin Pauli matrix vector and we define the functions

$$\Delta_0(\mathbf{r}) \pm \Delta_z(\mathbf{r}) = 2V \sum_{j=0}^2 \cos(\mathbf{G}_{2j} \cdot \mathbf{r} \mp \psi), \quad (13a)$$

$$\Delta_x(\mathbf{r}) \pm i\Delta_y(\mathbf{r}) = w \sum_{j=0}^2 e^{\pm i\mathbf{q}_j \cdot \mathbf{r}}, \quad (13b)$$

$\mathbf{q}_j = G_0/\sqrt{3}(\sin(2j\pi/3), -\cos(2j\pi/3))$ and $\mathbf{G}_j = G_0(\cos(j\pi/3), \sin(j\pi/3))$ where G_0 is the magnitude of the first-shell reciprocal lattice vectors, and (w, V, ψ) are three material-dependent phenomenological parameters. When $w, V > 0$ and $0 < \psi < \pi$, the vector field $\boldsymbol{\Delta}(\mathbf{r})$ has a topologically non-trivial real-space texture leading to a unit

real-space Chern number of $\mathbf{u}(\mathbf{r})$. We choose $(w, V, \psi) = (18\text{meV}, 9\text{meV}, 128^\circ)$ [48] though the choice of (w, V, ψ) should not affect our results as long as $\mathbf{u}(\mathbf{r})$ winds over the unit cell.

We numerically fix the U(1) gauge of $\tilde{\mathbf{u}}(\mathbf{r})$ so that the real-space Berry connection $\mathbf{A}_{ad}(\mathbf{r})$ is a specific solution to $\nabla \times \mathbf{A}_{ad} = B_{ad}(\mathbf{r}) = \mathbf{\Delta} \cdot (\partial_x \mathbf{\Delta} \times \partial_y \mathbf{\Delta})/2|\mathbf{\Delta}|^3$:

$$A_{ad}(\mathbf{r}) = A_{ad}^x(\mathbf{r}) + iA_{ad}^y(\mathbf{r}) = -i \begin{pmatrix} \tilde{u}_+^*(\mathbf{r}) & \tilde{u}_-^*(\mathbf{r}) \end{pmatrix} \begin{pmatrix} (\partial_x + i\partial_y)\tilde{u}_+(\mathbf{r}) \\ (\partial_x + i\partial_y)\tilde{u}_-(\mathbf{r}) \end{pmatrix} = -\frac{i(x+iy)}{2} + \sum_{\mathbf{G} \neq 0} \frac{B_{ad,\mathbf{G}}}{G_x - iG_y} e^{i\mathbf{G} \cdot \mathbf{r}}, \quad (14)$$

which satisfies the Coulomb gauge $\nabla \cdot \mathbf{A} = 0$. We note here that the real-space Berry curvature $B_{ad}(\mathbf{r})$ does not affect the magnetic field $B(\mathbf{r})$ in which our model Hamiltonian is based. To determine the quasiperiodicity of $\tilde{\mathbf{u}}(\mathbf{r})$ after the gauge fixing, we first note the discrete translational symmetry $\Delta(\mathbf{r} + \mathbf{R}) = e^{i\tau^z \mathbf{q}_0 \cdot \mathbf{R}} \Delta(\mathbf{r}) e^{-i\tau^z \mathbf{q}_0 \cdot \mathbf{R}}$ for arbitrary lattice vector \mathbf{R} , hence let

$$\tilde{\mathbf{u}}(\mathbf{r} + \mathbf{R}) = e^{i\sigma^z \mathbf{q}_0 \cdot \mathbf{R} + i\xi_{\mathbf{R}}(\mathbf{r})} \tilde{\mathbf{u}}(\mathbf{r}), \quad (15)$$

where $\xi_{\mathbf{R}}(\mathbf{r})$ is some smooth phase to be determined. This leads to the quasiperiodic boundary condition in the Berry connection $A_{ad}(\mathbf{r} + \mathbf{R}) = A_{ad}(\mathbf{r}) + (\partial_x + i\partial_y)\xi_{\mathbf{R}}(\mathbf{r})$. On the other hand, the far right-hand-side of Eq. (14) gives $A_{ad}(\mathbf{r} + \mathbf{R}) = A_{ad}(\mathbf{r}) - (i/2)(R_x + iR_y)$, which indicates that $\xi_{\mathbf{R}}(\mathbf{r}) = \mathbf{r} \times \mathbf{R}/2 + \theta_{\mathbf{R}}$ where $\theta_{\mathbf{R}}$ is \mathbf{r} -independent. Self-consistency of Eq. (15) requires that for any two lattice vectors \mathbf{R}_1 and \mathbf{R}_2 , $\xi_{\mathbf{R}_1 + \mathbf{R}_2}(\mathbf{r}) = \xi_{\mathbf{R}_2}(\mathbf{r} + \mathbf{R}_1) + \xi_{\mathbf{R}_1}(\mathbf{r}) + 2n\pi$ for some integer n , which means that $e^{i\theta_{\mathbf{R}_1 + \mathbf{R}_2}} = e^{i(\theta_{\mathbf{R}_1} + \theta_{\mathbf{R}_2} + \mathbf{R}_1 \times \mathbf{R}_2/2)}$. The general solution is $e^{i\theta_{\mathbf{R}}} = \eta_{\mathbf{R}} e^{i\mathbf{b} \cdot \mathbf{R}}$ for some constant vector \mathbf{b} . Similar analyses based on C_2 and C_3 symmetries fix \mathbf{b} to reciprocal lattice vectors, which can then be set to 0. Ultimately we have

$$\tilde{\mathbf{u}}(\mathbf{r} + \mathbf{R}) = \eta_{\mathbf{R}} e^{i(\frac{\mathbf{r} \times \mathbf{R}}{2} + \sigma^z \mathbf{q}_0 \cdot \mathbf{R})} \tilde{\mathbf{u}}(\mathbf{r}). \quad (16)$$

Finally we define $\mathbf{u}(\mathbf{r}) = e^{-i\sigma^z \mathbf{q}_0 \cdot \mathbf{R}} \tilde{\mathbf{u}}(\mathbf{r})$. Now combining $\mathbf{u}(\mathbf{r})$ with Eq. (10), we see that the transformed wave function $\phi_{n,\mathbf{k}s}(\mathbf{r})$ defined by the first equality of Eq. (11) has the exact Bloch periodicity with momentum \mathbf{k} . In practice, the truncation of reciprocal lattice summation in Eq. (11) can slightly violate the orthonormality between bands. We solve this problem by performing Gram-Schmidt orthonormalization on the transformed LL wave functions $\phi_{\mathbf{k}s}^{nLL}(\mathbf{r}) = \psi_{\mathbf{k}}^{nLL}(\mathbf{r}) u_s(\mathbf{r})$. To justify our algorithm, we have confirmed that the Berry curvature distribution $\Omega_{\mathbf{k}}$ and the quantum metric trace $\text{tr}g_{\mathbf{k}}$ computed under the transformed plane-wave basis agree perfectly both among different choices of (w, V, ψ) and with those computed from the original LL basis using the method described in Ref. [37].

We project un-screened Coulomb interactions to the highest band of the single-particle Hamiltonian Eq. (1) in the main text, hence we will drop the band index from now on, and perform exact diagonalization on the many-body Hamiltonian

$$H = \sum_{\mathbf{k}} \epsilon_{\mathbf{k}} c_{\mathbf{k}}^\dagger c_{\mathbf{k}} + \frac{1}{2} \sum_{\substack{\mathbf{k}_i, \mathbf{k}_j \\ \mathbf{k}_k, \mathbf{k}_l}} V_{ijkl} c_{\mathbf{k}_i}^\dagger c_{\mathbf{k}_j}^\dagger c_{\mathbf{k}_l} c_{\mathbf{k}_k}, \quad (17)$$

where $c_{\mathbf{k}}^\dagger(c_{\mathbf{k}})$ creates (destroys) a spin-less hole with momentum \mathbf{k} ; i, j, k, l are momentum labels, and V_{ijkl} is a two-particle matrix element that we compute using the plane-wave basis constructed in Eq. (11) and can be compactly written as

$$V_{ijkl} = \frac{1}{A} \left(\sum_{\mathbf{G}} \Lambda_{\mathbf{k}_1}^{q+\mathbf{G}} \Lambda_{\mathbf{k}_2}^{-q-\mathbf{G}} \frac{2\pi e^2}{\varepsilon(q+\mathbf{G})} \right). \quad (18)$$

Here, $q + \mathbf{G} = |\mathbf{q} + \mathbf{G}|$ is the momentum transfer, A is the area of the system and we make the standard choosing $V(\mathbf{q} = 0) = 0$. The form factors in Eq. (18) are defined as

$$\Lambda_{\mathbf{k}}^{q+\mathbf{G}} = \sum_{\mathbf{G}', s} z_{\mathbf{k}, \mathbf{G}', s}^* z_{\mathbf{k}+\mathbf{q}, \mathbf{G}'+\mathbf{G}, s}, \quad (19)$$

where the coefficients $z_{\mathbf{k}, \mathbf{G}, s}$ are obtained from Eq. (11). For all calculations presented in this work we have fixed $\varepsilon = 10$, which correspond to an interaction strength scale $e^2/\varepsilon\ell \approx 3.408 \hbar\omega_c$, for a sample with twist angle $\theta = 1.67^\circ$

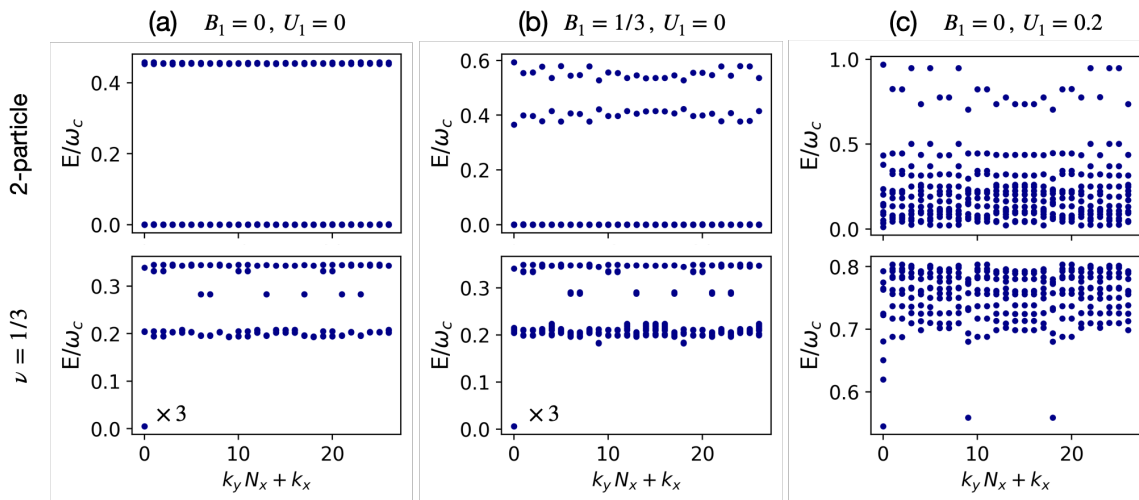


FIG. 3. LLL *vs.* AC band *vs.* non-ideal band for first Haldane pseudopotential interactions. Two-particle spectrum for (a) the LLL; (b) an AC (ideal) band; and (c) a generic adiabatic band. Both (a) and (b) display a highly degenerate zero-energy manifold. Many-body spectrum at $\nu = 1/3$ filling for (d) the LLL; (e) an AC (ideal) band; and (f) a generic adiabatic band. (d) and (e) display a three-fold degenerate ground zero-energy state in the same universality class as the Laughlin state, while (f) is in a CDW phase with non-zero ground state energy.

and lattice constant $a_0 = 0.3317$ nm [48].

To further confirm the validity of our numerical approach, in Fig. 3(a)-(c) we present many-body calculations for an idealized limit where the interaction consists only of the first Haldane pseudopotential, V_1 , in a system with 27 unit cells. We compare the two-particle and the $\nu = 1/3$ filling factor spectra for the (a) lowest Landau level ($B_1 = U_1 = 0$), (b) an ideal AC band ($B_1 \neq 0$, $U_1 = 0$), and (c) an adiabatic band ($B_1 = 0$, $U_1 \neq 0$). As expected for the LLL, the two-particle spectrum displays a highly-degenerate zero-energy ground state manifold, separated from a two-fold degenerate finite-energy branch. For the AC band, which is ideal, the zero-energy manifold persists but the finite-energy branch now splits into two and acquires a dispersion. This behavior is expected due to the non-trivial quantum geometry of the AC band [50]. In contrast, the two-particle spectrum for the non-ideal band is dense, as shown in Fig. 3(c). This indicates that adding the residual potential to the AC Hamiltonian indeed destroys the ideal band structure.

From Fig. 3(a)-(b) we see that the $\nu = 1/3$ spectra for the LLL and the ideal band look quite similar: There is a three-fold degenerate ground state at many-body momentum γ well separated from all excitations, which is characteristic of a Laughlin-like state for this system size. This is in agreement with the LLL and the AC band having ideal quantum geometry. Finally, from the $\nu = 1/3$ spectrum in Fig. 3(c) we see that the ground state has finite energy and that the three-fold degeneracy at γ is lifted, with two states with many-body momentum κ and κ' dropping down from the excited states to become nearly-degenerate with the lowest state at γ . For the studied system size, this level crossing is typical of a transition from the FCI to a charge density wave ground state.

In this work we are mostly interested in situations where the $\nu = 1/3$ many-body spectrum looks like in Figs. 3(a)-(b). In such cases the ground state is topologically-ordered and three-fold quasi-degenerate. The small energy-splitting between the three ground states is caused by the finite system size, but it should become zero in the thermodynamic limit. We define the many-body gap as the energy difference between the lowest-energy state that does not belong to the three-fold ground state manifold and the state with the highest energy within the ground state manifold. This is equivalent to taking the difference between the fourth and third lowest many-body energies if the system is in the FCI phase:

$$\Delta = \varepsilon_4 - \varepsilon_3. \quad (20)$$

Here we will focus mainly on system sizes 27 and 36, where the three-fold topological ground state appears at the γ momentum sector (in agreement with [81]) and the lowest excitation energies emerge at the κ/κ' sectors. Eq. (20) is what we plot in the main text figures to assess the stability of the FCI phase.

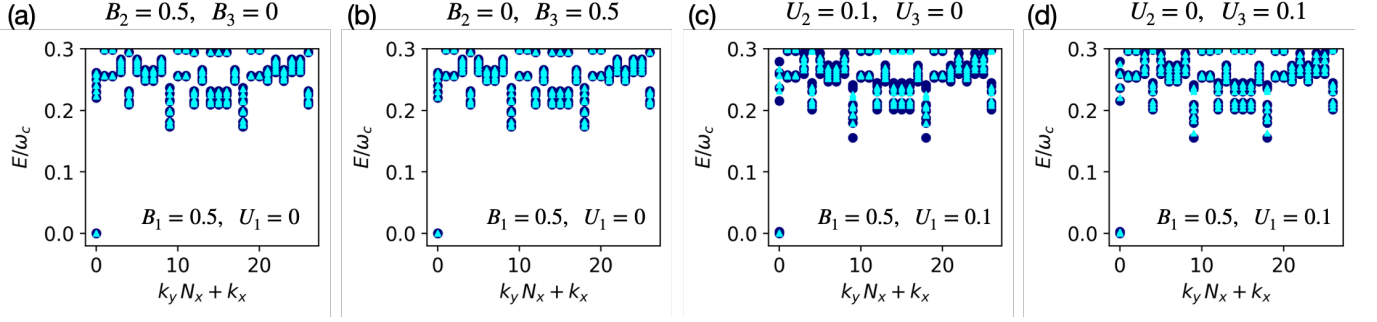


FIG. 4. (a)-(b) Comparison between many-body spectra for AC bands with only first harmonic $B_1 = 0.5$ (dark blue) and for AC bands including higher harmonics (a) $B_2 = 0.5$ and (b) $B_3 = 0.5$ (cyan.) (c)-(d) Comparison between many-body spectra for adiabatic bands with $B_1 = 0.5$ and $U_1 = 0.1$ and adiabatic bands with higher harmonics (c) $U_2 = 0.1$ and (d) $U_3 = 0.1$ (cyan.)

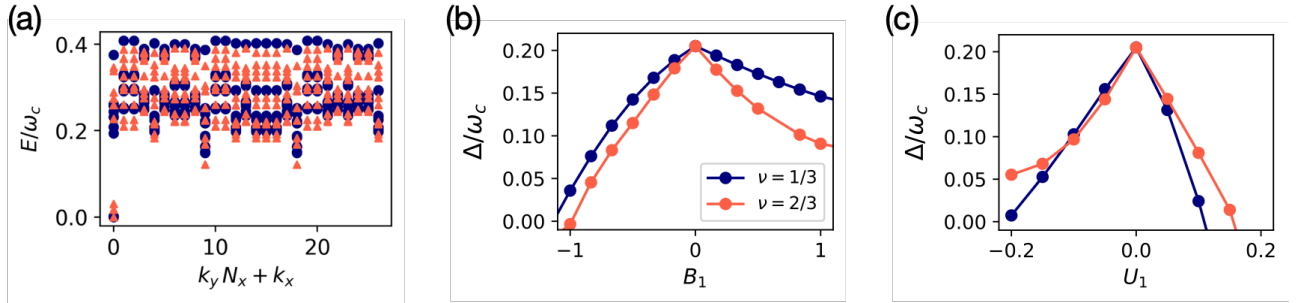


FIG. 5. (a) Comparison of many-body spectra for $\nu = 1/3$ and $\nu = 2/3$ filling factors, for $B_1 = 1$. Both ground states are FCIs but the many-body gaps differ. (b) Evolution of the many-body gap Δ as a function of B_1 , illustrating the particle-hole asymmetry due to the non-homogeneous Berry curvature. (c) Many-body gap for a band with $B_1 = 0$ as a function of U_1 , which also shows particle-hole asymmetry. Labels are the same as in (b).

We now present some additional ED results using the un-screened Coulomb interaction, which complement the ones presented in the main text. In Fig. 5 we show many-body spectra for different AC and adiabatic bands where we include only the first harmonics for the functions $B(\mathbf{r})$ and $U(\mathbf{r})$ and compare them with the spectra resulting from including higher-shell harmonics. The fact that the spectra in the two cases look almost identical justifies the approach we took of truncating the periodic functions that determine the adiabatic Hamiltonian to the first shell. In Fig. 5 we also compare many-body results for filling $\nu = 1/3$ (considered in the main text) with filling $\nu = 2/3$. Finally, in Fig. 6 we show results for the ground state momentum occupations for different bands. We see that $n(\mathbf{k})$ follows the distribution of the Berry curvature, with lower hole occupation in regions of peaked $\Omega_{\mathbf{k}}$.

Fourier expansions of some periodic functions

In this work we have considered a magnetic field with only non-vanishing first-shell Fourier coefficients, B_1 . The function $\chi(\mathbf{r})$ that enters in the AC band wave function is related to the magnetic field by $\nabla^2 \chi(\mathbf{r}) = B(\mathbf{r})$, hence its Fourier coefficients are related to those of the magnetic field via $\chi_{\mathbf{G}} = -B_{\mathbf{G}}/|\mathbf{G}|^2$ and we can write

$$\chi(\mathbf{r}) = \sum_{\mathbf{G}} \chi_{\mathbf{G}} e^{i\mathbf{G}\cdot\mathbf{r}} = \sum_{\mathbf{G}} \left(-\frac{B_1}{G_0^2} \right) e^{i\mathbf{G}\cdot\mathbf{r}}, \quad (21)$$

where we used that only the first-shell harmonics of the magnetic field are non-vanishing, and G_0 is the magnitude of the first-shell reciprocal lattice vectors. For all the derivations below we will take the harmonic B_1 as a perturbative parameter.

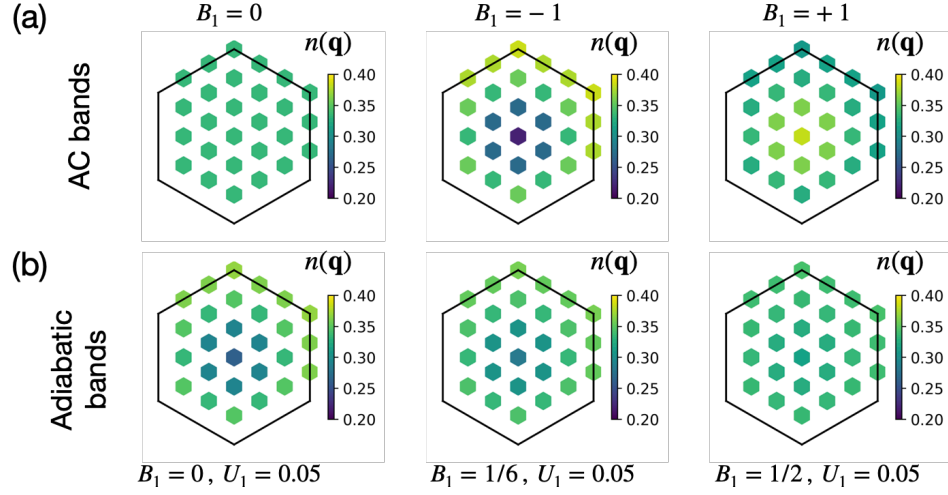


FIG. 6. Momentum occupation plots for (a) different ideal bands and (b) different adiabatic bands. For the LLL the occupation is constant $n(\mathbf{q}) \approx 0.33$, but once $B_1 \neq 0$ the occupation displays structure which is related to the Berry curvature distribution. For the non-ideal bands in the second row we see that the closest to constant occupation does not correspond to the band with $B_1 = 0$. The band with more homogeneous occupation is the one for which the many-body gap is larger. This illustrates the cancellation between contributions to the Berry curvature coming from $B(\mathbf{r})$ and $U(\mathbf{r})$ that we discuss in the main text.

The periodic functions $e^{\chi(\mathbf{r})}$ and $e^{2\chi(\mathbf{r})}$ can be written as

$$e^{\chi(\mathbf{r})} = 1 + \chi(\mathbf{r}) + \frac{1}{2}\chi^2(\mathbf{r}) + \dots = \sum_{\mathbf{G}} \varphi_{\mathbf{G}} e^{i\mathbf{G}\cdot\mathbf{r}}, \quad (22)$$

$$e^{2\chi(\mathbf{r})} = 1 + 2\chi(\mathbf{r}) + 2\chi^2(\mathbf{r}) + \dots = \sum_{\mathbf{G}} \Phi_{\mathbf{G}} e^{i\mathbf{G}\cdot\mathbf{r}}. \quad (23)$$

The coefficients $\varphi_{\mathbf{G}}$ and $\Phi_{\mathbf{G}}$ can be obtained from the Fourier expansion of

$$\chi^2(\mathbf{r}) = \sum_{\mathbf{G}, \mathbf{G}'} \chi_{\mathbf{G}} \chi_{\mathbf{G}'} e^{i(\mathbf{G}+\mathbf{G}')\cdot\mathbf{r}} = \sum_{\mathbf{G}} (\chi_{\mathbf{G}} \chi_{-\mathbf{G}} + 2\chi_{\mathbf{G}}^2 e^{i\mathbf{G}\cdot\mathbf{r}}) = 6\chi_1^2 + 2 \sum_{\mathbf{G} \neq 0} \chi_1^2 e^{i\mathbf{G}\cdot\mathbf{r}}, \quad (24)$$

which yields the following relations for the first two Fourier coefficients

$$\varphi_0 = 1 + 3\chi_1^2, \quad \varphi_1 = \chi_1 + \chi_1^2. \quad (25)$$

$$\Phi_0 = 1 + 12\chi_1^2, \quad \Phi_1 = 2\chi_1 + 4\chi_1^2. \quad (26)$$

Note that the functions $e^{\chi(\mathbf{r})}$ and $e^{2\chi(\mathbf{r})}$ have infinite non-vanishing Fourier coefficients, however given that $B_1 \ll 1$ we will truncate them to the first shell of harmonics. The AC many-body ground state wave functions involve products of $e^{\chi(\mathbf{r}_i)}$ and $e^{2\chi(\mathbf{r}_i)}$ over all N particles composing the system. These products can be truncated to first order in χ_1 as

$$\begin{aligned} \prod_{i=1}^N e^{\chi(\mathbf{r}_i)} &= \left(\sum_{\mathbf{G}} \varphi_{\mathbf{G}} e^{i\mathbf{G}\cdot\mathbf{r}_1} \right) \dots \left(\sum_{\mathbf{G}} \varphi_{\mathbf{G}} e^{i\mathbf{G}\cdot\mathbf{r}_N} \right) \approx \varphi_0^N + \varphi_0^{N-1} \left(\sum_{\mathbf{G} \neq 0} \varphi_1 e^{i\mathbf{G}\cdot\mathbf{r}_1} + \dots + \sum_{\mathbf{G} \neq 0} \varphi_1 e^{i\mathbf{G}\cdot\mathbf{r}_N} \right) + O(\varphi_1^2) \\ &\approx 1 + \sum_{i=1}^N \sum_{\mathbf{G} \neq 0} \chi_1 e^{i\mathbf{G}\cdot\mathbf{r}_i} + O(\chi_1^2) = 1 + \sum_{\mathbf{G} \neq 0} \chi_1 \rho_{\mathbf{G}} + O(\chi_1^2), \end{aligned} \quad (27)$$

and

$$\prod_{i=1}^N e^{2\chi(\mathbf{r}_i)} \approx 1 + \sum_{i=1}^N \sum_{\mathbf{G} \neq 0} 2\chi_1 e^{i\mathbf{G}\cdot\mathbf{r}_i} + O(\chi_1^2) = 1 + \sum_{\mathbf{G} \neq 0} 2\chi_1 \rho_{\mathbf{G}} + O(\chi_1^2). \quad (28)$$

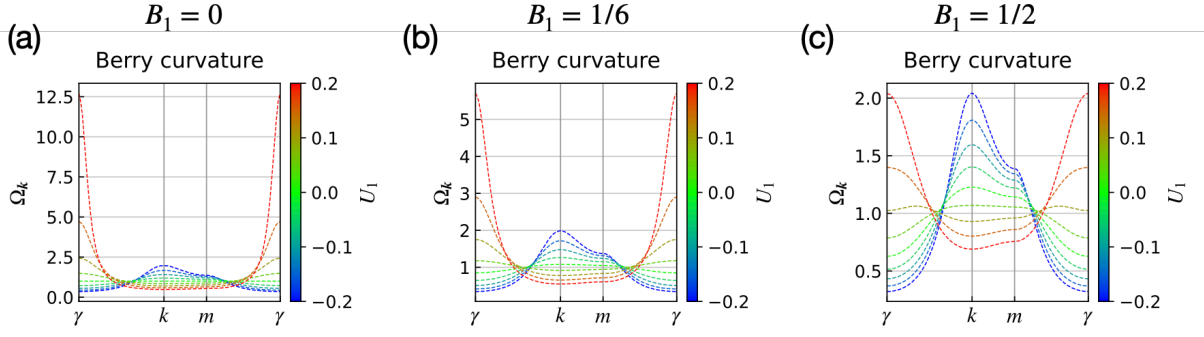


FIG. 7. Berry curvatures for different adiabatic bands. (a) $\Omega_{\mathbf{k}}$ for the LLL plus a residual potential. We see that $U_1 > 0$ leads to a Berry curvature peak at γ and $U_1 < 0$ leads to Berry curvature peaks at κ/κ' , which confirms our intuition obtained from Eq. (31). (b) and (c) show that a finite B_1 generically decreases the magnitude of the peaks of $\Omega_{\mathbf{k}}$.

Berry curvature of the Aharonov-Casher band and energy of the adiabatic band

From Eq. (4) in the main text, we see that the Berry curvature of the AC band can be expressed in terms of the Fourier coefficients $\Phi_{\mathbf{G}}$

$$\Omega_{\mathbf{k}} = \Omega_0 + \frac{1}{2} \nabla_{\mathbf{k}}^2 \ln \left(\sum_{\mathbf{G}} \Phi_{\mathbf{G}} \langle \psi_{\mathbf{k}}^{\text{LLL}} | e^{i \mathbf{G} \cdot \hat{\mathbf{r}}} | \psi_{\mathbf{k}}^{\text{LLL}} \rangle \right) = \Omega_0 + \frac{1}{2} \nabla_{\mathbf{k}}^2 \ln \left(\sum_{\mathbf{G}} \Phi_{\mathbf{G}} \bar{\eta}_{\mathbf{G}} \lambda_{\mathbf{G}} e^{i \ell^2 \mathbf{k} \times \mathbf{G}} \right), \quad (29)$$

where the magnetic form factor is $\lambda_{\mathbf{G}} = e^{-|\mathbf{G}|^2 \ell^2 / 4}$, $\bar{\eta}_{\mathbf{G}} = 1$ if $\mathbf{G}/2$ belongs to the reciprocal lattice and $\bar{\eta}_{\mathbf{G}} = -1$ otherwise. If we keep only terms up to order χ_1 , we obtain

$$\begin{aligned} \Omega_{\mathbf{k}} &\approx \Omega_0 + \frac{1}{2} \nabla_{\mathbf{k}}^2 \ln \left(1 - \sum_{j=1}^6 2\chi_1 \lambda_1 e^{i \mathbf{k} \cdot \mathbf{R}_j} + O(\chi_1^2) \right) \approx \Omega_0 + \frac{1}{2} \nabla_{\mathbf{k}}^2 \left(- \sum_{j=1}^6 2\chi_1 \lambda_1 e^{i \mathbf{k} \cdot \mathbf{R}_j} + O(\chi_1^2) \right) \\ &= \Omega_0 - \frac{a^2 B_1 \lambda_1}{G_0^2} \sum_{j=1}^6 e^{i \mathbf{k} \cdot \mathbf{R}_j} + O(B_1^2) = \Omega_0 - \frac{4\pi \ell^2 B_1 e^{-G_0^2 \ell^2 / 4}}{\sqrt{3} G_0^2} \sum_{j=1}^6 e^{i \mathbf{k} \cdot \mathbf{R}_j} + O(B_1^2). \end{aligned} \quad (30)$$

In the previous expressions the vectors \mathbf{R}_j belong to the first shell of lattice vectors. This is Eq. (7) in the main text. From this linear expansion in B_1 we see that the Berry curvature is peaked at κ/κ' for $B_1 > 0$ and peaked at γ for $B_1 < 0$, as seen in Fig. 1(d) in the main text.

Once the residual potential is introduced, it induces a finite band width on the AC band. Focusing on the case $B_1 = 0$, we can estimate the corrections to the band energy introduced by $U(\mathbf{r})$ as

$$\delta E_{\mathbf{k}} = \frac{\langle \psi_{\mathbf{k}}^{\text{LLL}} | U(\mathbf{r}) | \psi_{\mathbf{k}}^{\text{LLL}} \rangle}{\langle \psi_{\mathbf{k}}^{\text{LLL}} | \psi_{\mathbf{k}}^{\text{LLL}} \rangle} = \langle \psi_{\mathbf{k}}^{\text{LLL}} | \sum_{\mathbf{G} \neq 0} U_1 e^{i \mathbf{G} \cdot \mathbf{r}} | \psi_{\mathbf{k}}^{\text{LLL}} \rangle = -U_1 e^{-G_0^2 \ell^2 / 4} \sum_{j=1}^6 e^{i \mathbf{k} \cdot \mathbf{R}_j}. \quad (31)$$

We see that for $U_1 > 0$ the adiabatic band will have a single dip at γ and for $U_1 < 0$ there are two dips at κ/κ' . Because we are working in the hole language, these dips will coincide with the peaks of the Berry curvature induced by $U(\mathbf{r})$, because those are the regions where band mixing is more important. Fig. 7 confirms this behavior: $U_1 > 0$ corresponds to $\Omega_{\mathbf{k}}$ peaked at γ , while $U_1 < 0$ will lead to $\Omega_{\mathbf{k}}$ peaked at κ/κ' . From Eq. (31) we expect that for a finite positive B_1 (the case studied in the main text) the Berry curvature is less pronounced than in the case of no periodic magnetic field, because the location of the maxima and minima induced by $B(\mathbf{r})$ are opposite to those induced by $U(\mathbf{r})$. This is also confirmed numerically in Fig. 7.

Approximation for the magnetoroton gap

In this section we will focus on AC bands that are perturbatively close to the LLL, namely bands where the oscillating piece of the magnetic field is small in magnitude, $|B_1| \ll 1$. We are interested in calculating the $\nu = 1/3$ -filling

magnetoroton gap

$$\Delta^{AC}(\mathbf{q}) = E^{AC}(\mathbf{q}) - E_0^{AC}, \quad (32)$$

where E_0^{AC} is the ground state energy of the AC band and $E^{AC}(\mathbf{q})$ its energy of the lowest neutral excitation at momentum \mathbf{q} . In particular we want to compare Eq. (32) with the LLL magnetoroton gap

$$\Delta^{LLL}(\mathbf{q}) = E^{LLL}(\mathbf{q}) - E_0^{LLL}, \quad (33)$$

where E_0^{LLL} is the ground state energy of the LLL and $E^{LLL}(\mathbf{q})$ the magnetoroton energy. We assume that the many-body ground state of the AC band, denoted as Ψ_0^{AC} , is related to the many-body ground state of the LLL, Ψ_0^{LLL} , via

$$\Psi_0^{AC}(\{\mathbf{r}_i\}) = \left(e^{\sum_{i=1}^N \chi(\mathbf{r}_i)} \right) \Psi_0^{LLL}(\{\mathbf{r}_i\}) = e^X \Psi_0^{LLL}(\{\mathbf{r}_i\}). \quad (34)$$

This relation is exact for arbitrary B_1 and for a first Haldane pseudopotential interaction. We expect that for the Coulomb interaction Eq. (34) is a reasonable approximation for the ground state, as long as $|B_1| \ll 1$. We can estimate the AC ground state energy by

$$E_0^{AC} = \frac{\langle \Psi_0^{AC} | H_{\text{int}} | \Psi_0^{AC} \rangle}{\langle \Psi_0^{AC} | \Psi_0^{AC} \rangle} = \frac{\langle e^X H_{\text{int}} e^X \rangle_0^{LLL}}{\langle e^{2X} \rangle_0^{LLL}}, \quad (35)$$

where $\langle \dots \rangle_0^{LLL} \equiv \langle \Psi_0^{LLL} | \dots | \Psi_0^{LLL} \rangle$. By using the expansions introduced in the previous section the numerator is

$$\begin{aligned} \langle e^X H_{\text{int}} e^X \rangle_0^{LLL} &\approx \langle H_{\text{int}} \rangle_0^{LLL} + \sum_{\mathbf{G} \neq 0} \chi_1 \langle H_{\text{int}} \bar{\rho}_{\mathbf{G}} + \bar{\rho}_{\mathbf{G}} H_{\text{int}} \rangle_0^{LLL} + O(\chi_1^2) \\ &= E_0^{LLL} + 2E_0^{LLL} \sum_{\mathbf{G} \neq 0} \chi_1 \langle \bar{\rho}_{\mathbf{G}} \rangle_0^{LLL} + O(\chi_1^2), \end{aligned} \quad (36)$$

and similarly the denominator is

$$\langle e^{2X} \rangle_0^{LLL} = 1 + 2 \sum_{\mathbf{G} \neq 0} \chi_1 \langle \bar{\rho}_{\mathbf{G}} \rangle_0^{LLL} + O(B_1^2) \approx 1 + O(B_1^2). \quad (37)$$

Note that due to continuous translational symmetry $\langle \bar{\rho}_{\mathbf{G} \neq 0} \rangle_0^{LLL} = 0$, the lowest-order correction to E_0^{LLL} induced by the non-homogeneity of the magnetic field is quadratic in B_1 ,

$$E_0^{AC} \approx E_0^{LLL} + O(B_1^2). \quad (38)$$

In Fig. 8 we show the evolution of the three topological ground states at $\nu = 1/3$ -filling with B_1 . The small separation as compared to the other energy scales supports the result in Eq. (38).

We now want to estimate the energy of the neutral excitations on top of the AC ground state $|\Psi_0^{AC}\rangle$. We define them in the *single mode approximation* (SMA) [82, 83], by applying the AC-projected density operator

$$|\tilde{\Psi}_{\mathbf{q}}^{AC}\rangle = \frac{1}{\sqrt{N}} \tilde{\rho}_{\mathbf{q}} |\Psi_0^{AC}\rangle = \frac{1}{\sqrt{N}} \tilde{\rho}_{\mathbf{q}} e^X |\Psi_0^{LLL}\rangle. \quad (39)$$

We use the notation \tilde{O} to refer to an operator projected to the AC band and \bar{O} for the operator projected to the LLL. There is an alternative way to define the neutral excitations of the AC ground state, via the action of the LLL-projected density

$$|\Psi_{\mathbf{q}}^{AC}\rangle = \frac{1}{\sqrt{N}} e^{X(\{\mathbf{r}_i\})} |\Psi_{\mathbf{q}}^{LLL}\rangle = \frac{1}{\sqrt{N}} e^X \bar{\rho}_{\mathbf{q}} |\Psi_0^{LLL}\rangle. \quad (40)$$

Eqs. (39) and (40) span the same Hilbert space and for simplicity we will work with the basis defined in Eq. (40).

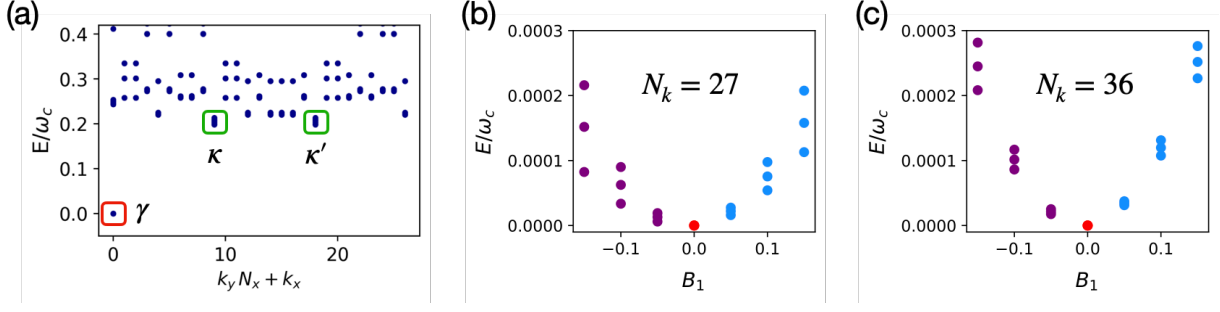


FIG. 8. (a) Many-body spectrum for an AC band with $B_1 = 0.1$ and $N_k = 27$ unit cells. The three quasi-degenerate topological ground states are at γ and are indicated in red. The lowest excitations are located at κ/κ' and are indicated in green. (b)-(c) Evolution of the three topological ground states as a function of B_1 for systems with 27 and 36 unit cells, respectively. Note that for $B_1 \neq 0$ the energy change with respect to the LLL ground state energy is 10^3 times smaller than the many-body gap. Note that for a given B_1 , the ground state splitting decreases with system size, indicating that the three states are degenerate in the thermodynamic limit.

One can note that states $|\Psi_{\mathbf{q}}^{AC}\rangle$ and $|\Psi_{\mathbf{k}}^{AC}\rangle$ are not necessarily orthogonal, as they can be coupled by a reciprocal lattice vector. This implies that the structure factor is not purely diagonal in a basis of reciprocal lattice vectors

$$\langle \Psi_{\mathbf{k}}^{AC} | \Psi_{\mathbf{q}}^{AC} \rangle = \frac{1}{N} \langle \bar{\rho}_{-\mathbf{k}} e^{2X} \bar{\rho}_{\mathbf{q}} \rangle_0^{LLL} \approx \frac{1}{N} \left(\langle \bar{\rho}_{-\mathbf{k}} \bar{\rho}_{\mathbf{q}} \rangle_0^{LLL} \delta_{\mathbf{k},\mathbf{q}} + 2 \sum_{\mathbf{G} \neq 0} \chi_1 \langle \bar{\rho}_{-\mathbf{k}} \bar{\rho}_{\mathbf{G}} \bar{\rho}_{\mathbf{q}} \rangle_0^{LLL} \delta_{\mathbf{k},\mathbf{q}+\mathbf{G}} + O(\chi_1^2) \right), \quad (41)$$

where we have used the expansion in Eq. (28). The lowest-order off-diagonal elements of Eq. (41) are the three-point density correlation functions of the LLL ground state. Similarly, the matrix elements of the interacting Hamiltonian are given by

$$\begin{aligned} \langle \Psi_{\mathbf{k}}^{AC} | H_{\text{int}} | \Psi_{\mathbf{q}}^{AC} \rangle &= \frac{1}{N} \langle \bar{\rho}_{-\mathbf{k}} e^X H_{\text{int}} e^X \bar{\rho}_{\mathbf{q}} \rangle_0^{LLL} \\ &\approx \frac{1}{N} \left(\langle \bar{\rho}_{-\mathbf{k}} H_{\text{int}} \bar{\rho}_{\mathbf{q}} \rangle_0^{LLL} \delta_{\mathbf{k},\mathbf{q}} + \sum_{\mathbf{G} \neq 0} \chi_1 (\langle \bar{\rho}_{-\mathbf{k}} \bar{\rho}_{\mathbf{G}} H_{\text{int}} \bar{\rho}_{\mathbf{q}} \rangle_0^{LLL} + \langle \bar{\rho}_{-\mathbf{k}} H_{\text{int}} \bar{\rho}_{\mathbf{G}} \bar{\rho}_{\mathbf{q}} \rangle_0^{LLL}) \delta_{\mathbf{k},\mathbf{q}+\mathbf{G}} + O(\chi_1^2) \right), \end{aligned} \quad (42)$$

where we have used Eq. (27) for the truncation in the second line. We see that the off-diagonal elements consist of expectation values of five density operators in the LLL ground state. The energy of the neutral excitation for a given momentum \mathbf{q} in the Brillouin zone, $E^{AC}(\mathbf{q})$, can be estimated by solving the generalized eigenvalue problem

$$\sum_{\mathbf{G}} \langle \Psi_{\mathbf{q}+\mathbf{G}'}^{AC} | H_{\text{int}} | \Psi_{\mathbf{q}+\mathbf{G}}^{AC} \rangle u_{\mathbf{q},\mathbf{G}} = E^{AC}(\mathbf{q}) \sum_{\mathbf{G}} \langle \Psi_{\mathbf{q}+\mathbf{G}'}^{AC} | \Psi_{\mathbf{q}+\mathbf{G}}^{AC} \rangle u_{\mathbf{q},\mathbf{G}}, \quad (43)$$

where $u_{\mathbf{q},\mathbf{G}}$ is a generalized eigenvector. Even with the truncations obtained in Eqs. (41)-(42), solving the generalized eigenvalue problem would require a numerical calculation of several n -point correlation functions of the Laughlin state.

The condition of one flux quantum per unit cell, $2\pi\ell^2 = A_{\text{UC}}$, results in the minimum of the LLL magnetoroton excitation being approximately at the edges of the Brillouin zone defined by the periodicity of the magnetic field. When $B_1 \neq 0$, we observe from our numerical calculations that the lowest-energy excitation is at the κ/κ' points in the Brillouin zone. Using this fact we will simplify the problem in Eq. (43) by estimating magnetoroton energy only at the κ/κ' points, where the excitation minimum is located. From Eqs. (41) and (42) we see that only SMA states that differ by a reciprocal lattice vector are related, hence Ψ_{κ}^{AC} and $\Psi_{\kappa'}^{AC}$ are decoupled and we can focus on only the three κ points, that we denote by κ_i , with $i = 1, 2, 3$ and are related by C_3 -symmetry. The eigenvalue problem truncated to the three κ_i points reduces to

$$\begin{pmatrix} \bar{V}_0(\kappa_1) & \chi_1 \bar{V}_{1\mathbf{G}_0,\mathbf{G}_4}^{\kappa_1} & \chi_1 \bar{V}_{1\mathbf{G}_0,\mathbf{G}_5}^{\kappa_1} \\ \chi_1 \bar{V}_{1\mathbf{G}_4,\mathbf{G}_0}^{\kappa_1} & \bar{V}_0(\kappa_2) & \chi_1 \bar{V}_{1\mathbf{G}_4,\mathbf{G}_5}^{\kappa_1} \\ \chi_1 \bar{V}_{1\mathbf{G}_5,\mathbf{G}_0}^{\kappa_1} & \chi_1 \bar{V}_{1\mathbf{G}_5,\mathbf{G}_4}^{\kappa_1} & \bar{V}_0(\kappa_3) \end{pmatrix} u_{\kappa_1} = E(\kappa_1) \begin{pmatrix} \bar{S}_0(\kappa_1) & \chi_1 \bar{S}_{1\mathbf{G}_0,\mathbf{G}_4}^{\kappa_1} & \chi_1 \bar{S}_{1\mathbf{G}_0,\mathbf{G}_5}^{\kappa_1} \\ \chi_1 \bar{S}_{1\mathbf{G}_4,\mathbf{G}_0}^{\kappa_1} & \bar{S}_0(\kappa_2) & \chi_1 \bar{S}_{1\mathbf{G}_4,\mathbf{G}_5}^{\kappa_1} \\ \chi_1 \bar{S}_{1\mathbf{G}_5,\mathbf{G}_0}^{\kappa_1} & \chi_1 \bar{S}_{1\mathbf{G}_5,\mathbf{G}_4}^{\kappa_1} & \bar{S}_0(\kappa_3) \end{pmatrix} u_{\kappa_1}. \quad (44)$$

The reciprocal lattice vectors \mathbf{G}_i are indicated in Fig. 9(a) below, $\bar{S}_0(\mathbf{k}) = \langle \bar{\rho}_{-\mathbf{k}} \bar{\rho}_{\mathbf{k}} \rangle_0^{LLL}$ is the projected structure factor and $\bar{V}_0(\mathbf{k}) = \langle \bar{\rho}_{-\mathbf{k}} H_{\text{int}} \bar{\rho}_{\mathbf{k}} \rangle_0^{LLL}$ is an interaction matrix element calculated on the LLL ground state, which due to the C_3 -symmetry are all equal, $S_0 = \bar{S}_0(\boldsymbol{\kappa}_i)$ and $\bar{V}_0 = V_0(\boldsymbol{\kappa}_i)$. We have also defined

$$\bar{V}_1^{\mathbf{k}}_{\mathbf{G},\mathbf{G}'} = \frac{1}{N} \sum_{\tilde{\mathbf{G}}} (\langle \bar{\rho}_{-\mathbf{k}-\tilde{\mathbf{G}}} \bar{\rho}_{\tilde{\mathbf{G}}} H_{\text{int}} \bar{\rho}_{\mathbf{k}+\mathbf{G}'} \rangle_0^{LLL} + \langle \bar{\rho}_{-\mathbf{k}-\tilde{\mathbf{G}}} H_{\text{int}} \bar{\rho}_{\tilde{\mathbf{G}}} \bar{\rho}_{\mathbf{k}+\mathbf{G}'} \rangle_0^{LLL}) \equiv V_1, \quad (45)$$

$$\bar{S}_1^{\mathbf{k}}_{\mathbf{G},\mathbf{G}'} = \frac{2}{N} \sum_{\tilde{\mathbf{G}}} \langle \bar{\rho}_{-\mathbf{k}-\tilde{\mathbf{G}}} \bar{\rho}_{\tilde{\mathbf{G}}} \bar{\rho}_{\mathbf{k}+\mathbf{G}'} \rangle_0^{LLL} \equiv S_1. \quad (46)$$

The off-diagonal elements in Eq. (44) can be related by C_3 -symmetry, which allows us to write the problem in a more compact form,

$$\begin{pmatrix} V_0 & V_1^* & V_1 \\ V_1 & V_0 & V_1^* \\ V_1^* & V_1 & V_0 \end{pmatrix} u_{\boldsymbol{\kappa}_1} = E^{AC}(\boldsymbol{\kappa}_1) \begin{pmatrix} S_0 & S_1^* & S_1 \\ S_1 & S_0 & S_1^* \\ S_1^* & S_1 & S_0 \end{pmatrix} u_{\boldsymbol{\kappa}_1}. \quad (47)$$

The three eigenvalues of this problem are

$$E_s^{AC}(\boldsymbol{\kappa}_1) = \frac{V_0 + 2\chi_1 \text{Re}V_1}{S_0 + 2\chi_1 \text{Re}S_1}, \quad E_{d\pm}^{AC}(\boldsymbol{\kappa}_1) = \frac{V_0 + 2\chi_1 \text{Re}(V_1 e^{\pm i \frac{2\pi}{3}})}{S_0 + 2\chi_1 \text{Re}(S_1 e^{\pm i \frac{2\pi}{3}})}. \quad (48)$$

Working in the limit $|\chi_1| \ll 1$ we can approximate the first eigenvalue as

$$\begin{aligned} E_s^{AC}(\boldsymbol{\kappa}_1) &= \left(\frac{V_0 + 2\chi_1 \text{Re}V_1}{S_0} \right) \left(1 + \frac{2\chi_1 \text{Re}S_1}{S_0} \right)^{-1} \\ &\approx \left(\frac{V_0 + 2\chi_1 \text{Re}V_1}{S_0} \right) \left(1 - \frac{2\chi_1 \text{Re}S_1}{S_0} \right) \\ &= \frac{V_0}{S_0} + \frac{2\chi_1 \text{Re}V_1}{S_0} - \frac{2\chi_1 V_0 \text{Re}S_1}{S_0^2} + O(\chi_1^2) \\ &= E_0^{LLL} + \Delta^{LLL}(\boldsymbol{\kappa}_1) + \frac{2B_1}{G_0^2 S_0} \left[\frac{V_0 \text{Re}S_1}{S_0} - \text{Re}V_1 \right] + O(B_1^2). \end{aligned} \quad (49)$$

In the last line we have used that $\chi_1 = -B_1/G_0^2$ and that V_0/S_0 is the energy of the SMA state in the LLL to first order in B_1 , this is $V_0/S_0 = E_0^{LLL} + \Delta^{LLL}(\boldsymbol{\kappa}_1) + O(B_1^2)$. Similarly, the other two eigenvalues in the limit $|\chi_1| \ll 1$ are approximated as

$$\begin{aligned} E_{d\pm}^{AC}(\boldsymbol{\kappa}_1) &= \left(\frac{V_0 - \chi_1 [\text{Re}V_1 \mp \sqrt{3}\text{Im}V_1]}{S_0} \right) \left(1 - \frac{\chi_1 [\text{Re}S_1 \mp \sqrt{3}\text{Im}S_1]}{S_0} \right)^{-1} \\ &\approx \left(\frac{V_0 - \chi_1 [\text{Re}V_1 \mp \sqrt{3}\text{Im}V_1]}{S_0} \right) \left(1 + \frac{\chi_1 [\text{Re}S_1 \mp \sqrt{3}\text{Im}S_1]}{S_0} \right) \\ &= \frac{V_0}{S_0} + \chi_1 \left(-\frac{\text{Re}V_1}{S_0} + \frac{V_0 \text{Re}S_1}{S_0^2} \right) \pm \chi_1 \left(\frac{\sqrt{3}\text{Im}V_1}{S_0} - \frac{\sqrt{3}V_0 \text{Im}S_1}{S_0^2} \right) + O(\chi_1^2) \\ &= E_0^{LLL} + \Delta^{LLL}(\boldsymbol{\kappa}_1) - \frac{B_1}{G_0^2 S_0} \left[\frac{V_0 \text{Re}S_1}{S_0} - \text{Re}V_1 \right] \pm \frac{\sqrt{3}B_1}{G_0^2 S_0} \left[\frac{V_0 \text{Im}S_1}{S_0} - \text{Im}V_1 \right] + O(B_1^2). \end{aligned} \quad (50)$$

We define $\alpha = [V_0 \text{Re}S_1/S_0 - \text{Re}V_1]/G_0^2 S_0$ and $\beta = [V_0 \text{Im}S_1/S_0 - \text{Im}V_1]/G_0^2 S_0$, so we can compactly write the three eigenvalues as

$$E_s^{AC}(\boldsymbol{\kappa}_1) \approx E_0^{AC} + \Delta^{LLL}(\boldsymbol{\kappa}_1) + 2\alpha B_1, \quad \text{and} \quad E_{d\pm}^{AC}(\boldsymbol{\kappa}_1) \approx E_0^{AC} + \Delta^{LLL}(\boldsymbol{\kappa}_1) - \alpha B_1 \pm \beta B_1. \quad (51)$$

From the previous expressions we see that for $B_1 > 0$ the lowest eigenvalue is $E_{d-}^{AC}(\boldsymbol{\kappa}_1)$, and the corresponding magnetoroton gap, to first order in B_1 , is

$$\Delta^{AC}(\boldsymbol{\kappa}_1) \approx E_{d\pm}^{AC}(\boldsymbol{\kappa}_1) - E_0^{AC} = \Delta^{LLL}(\boldsymbol{\kappa}_1) - (\alpha + \beta)|B_1|, \quad \text{for } B_1 > 0. \quad (52)$$

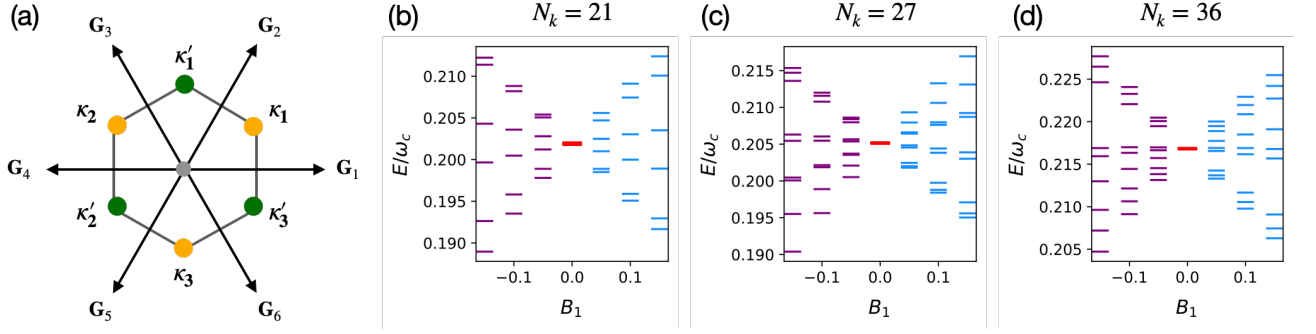


FIG. 9. (a) Schematic illustration of our minimal model for the magnetorotons at the corners of the Brillouin zone. The κ and κ' points are decoupled and degenerate in energy. (b),(c),(d) Energy of excitations at the κ -point, with respect to the ground state energy, for different system sizes and as a function of B_1 . For the system with 21 unit cells the three topological ground states are in different momentum sectors, hence there are only 6 low-energy magnetorotons at κ . For system sizes 27 and 36, the three ground states are in the same sector, resulting into 9 magnetoroton excitations at κ . The lowest excitation has consistently lower energy for $B_1 < 0$ than for $B_1 > 0$ across all system sizes.

In contrast, when $B_1 < 0$, the lowest eigenvalue is the singlet $E_s(\kappa_1)$ and the estimated magnetoroton gap to first order in B_1 is

$$\Delta^{AC}(\kappa_1) \approx E_s^{AC}(\kappa_1) - E_0^{AC} = \Delta^{LLL}(\kappa_1) - 2\alpha|B_1|, \quad \text{for } B_1 < 0. \quad (53)$$

Our model captures the fact that the energy of the lowest neutral excitation at κ is smaller for an AC band with $B_1 \neq 0$ than for the LLL, as observed in Fig. 1(c) in the main text. In addition, the difference in the slope of the magnetoroton for $B_1 > 0$ and $B_1 < 0$ is explained by Eqs. (52) and (53).

The ED calculations presented in the main text are performed by applying periodic boundary conditions, hence the states live on a torus. This results in a three-fold quasi-degenerate topological ground state. The single mode approximation at κ_i can be built on top of each topological ground state, which means that the full set of low-energy neutral excitations at κ_i consists of nine states, three excitations for each ground state. If there were no coupling between the neutral excitations obtained from each topological ground state, we would observe three sets of three-fold degenerate excitations and this is what we expect to happen in the thermodynamic limit. However, the coupling between different neutral excitations is non-vanishing for finite size systems, resulting in splittings between the nine energy levels at κ/κ' . In Fig. 9 we plot the energies of the lowest nine (or six) many-body states at κ , the corner of the Brillouin zone, as a function of B_1 and for different system sizes. We see that the splitting is almost negligible at $B_1 = 0$. For finite B_1 we observe a splitting of the energy levels, partly due to the mechanism described by Eq. (47), and partly due to mixing between different topological sectors. However, we observe that for $B_1 > 0$ the two lowest energy excitations are close in energy, in contrast to $B_1 < 0$, where there is a single lowest-energy excitation. Besides, the lowest neutral excitation has consistently lower energy for $B_1 < 0$ than for $B_1 > 0$. These results at different system sizes support the situation $\alpha > 0$, and $\alpha > \beta$. The specific values of α and β can be computed, for instance, via Monte Carlo simulations in the plasma analogy.